Supplementary Information

Self-assembled molybdenum disulfide nanoflowers regulated by lithium sulfate for high performance supercapacitors

Yunan Li,[*ab] Yang Sun,[a] Sen Zhang,[a] Xueling Wu,[a] Meng Song,[a] Mingli Jiao,[a] Qi Qin,[*a] and Liwei Mi[*b]

[a]School of Materials and Chemical Engineering, Zhongyuan University of Technology, Zhengzhou 450007, China

[b]Center for Advanced Materials Research, Henan Key Laboratory of Functional Salt Materials, Zhongyuan University of Technology, Zhengzhou 450007, China

* Corresponding authors.

E-mail addresses: yunanli@zut.edu.cn (Y. Li), qq@zut.edu.cn (Q. Qin), mlwzzu@163.com (L. Mi).

1. Experimental

1.1. Preparation of molybdenum disulfide nanoflowers regulated by lithium sulfate (L-MoS$_2$)

L-MoS$_2$ was synthesized by one-step hydrothermal reaction. Typically, 1 mmol ammonium molybdate tetrahydrate ($(NH_4)_6Mo_7O_{24} \cdot 4H_2O$, 1236 mg), 30 mmol thiourea ($(NH_2)_2CS$, 2284 mg), and 5 mmol lithium sulfate monohydrate ($Li_2SO_4 \cdot H_2O$, 640 mg) was dissolved into 20 mL of water under magnetic stirring for 30 min. The precursor solution was then transferred into a 25 mL Teflon-lined stainless-steel autoclave and kept at 180 °C for 24 h. After cooled down naturally to room temperature, the resultant precipitate was collected by centrifugation, washed with water and absolute ethanol several times, respectively, and finally dried at 60 °C under vacuum. The obtained sample was denoted as L-MoS$_2$. Keeping other reaction conditions unchanged, when the amount of $Li_2SO_4 \cdot H_2O$ added was respectively 2.5 mmol and 7.5 mmol, the obtained sample was denoted as L-MoS$_2$-2.5, and MnP-MoS$_2$-7.5, respectively. For comparison, Pure MoS$_2$ was prepared by following the same procedure without adding $Li_2SO_4 \cdot H_2O$.

1.2. Characterization

The morphologies of the samples were examined by a scanning electron microscope (SEM, ZEISS Sigma 300) and a transmission electron microscope (TEM, JEOL JEM-F200). The structure of the samples was studied by an X-ray diffractometer (XRD; Ultima-IV) with Cu Kα radiation ($\lambda = 0.15141$ nm). X-ray photoelectron spectroscopy (XPS, Thermo Scientific K-Alpha) was measured with a monochromatic Al Kα X-ray source ($hv = 1486.6$ eV). The specific surface area and pore size distribution was derived from nitrogen adsorption/desorption isotherms (Micromeritics ASAP 2460) at 77 K using the Brunauer-Emmett-Teller (BET) method and Barrett-Joyner-Halenda (BJH) model, respectively. The conductivity was measured with a multifunctional digital four-probe tester (ST2258C).

1.3. Electrochemical measurements

All the electrochemical tests were carried out using 2 M KOH as the electrolyte. The working electrode was prepared by mixing the obtained sample as the active material, polyvinylidene fluoride as the binder and acetylene black as the conductive agent with a weight ratio of 8:1:1 in N-methyl-2-pyrrolidone solvent. Then the slurry was spread on nickel foam, dried overnight at the temperature of 80 °C. Finally, a 10 MPa pressure was applied on the electrode. The active material mass for each electrode was about 2~3 mg cm^{-2}. For three-electrode system, Pt foil and Hg/HgO electrode was used as the counter electrode and the reference electrode, respectively. The symmetric supercapacitors (SSCs) were assembled using the two-electrode system. To assemble the SSCs, the L-MoS$_2$ slurry was coated on nickel foam to serve as both positive and negative electrode (mass loading: 2~3 mg cm^{-2}). After drying, two identical L-MoS$_2$ electrodes were separated by polypropylene diaphragm and then fixed with cover glass and elastic band. During electrochemical tests, the SSC device was immersed in a 2 M KOH electrolyte solution. The photographs of the SSC device and two-electrode test system are shown below.
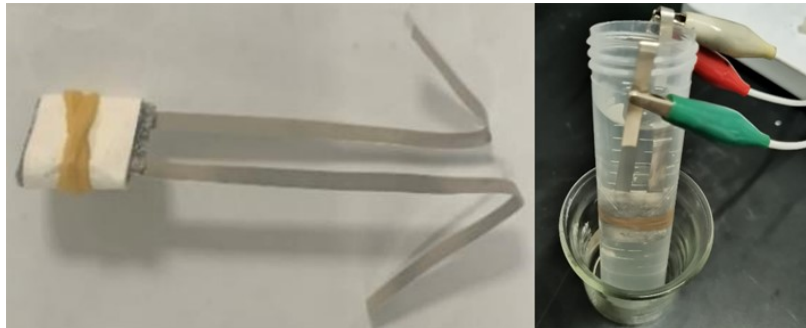
The photographs of the SSC device (left) and two-electrode test system (right).

Cyclic voltammetry (CV), galvanostatic charge-discharge (GCD) and electrochemical impedance spectroscopy (EIS, frequency: 0.1 Hz–100 kHz) curves were obtained by using a CHI 660E electrochemical workstation at room temperature. The specific capacitance was calculated according to the GCD curves by using the eqn S1:

$$C = \frac{I\Delta t}{m\Delta V} \qquad (S1)$$

Where C represents the specific capacitance (F g^{-1}), I (A) refers to the discharge current,

ΔV (V) represents the potential change within the discharge time Δt (s), m (g) corresponds to the mass of active material in three-electrode system and total mass of active material in two-electrode system.

The energy density E (W h kg^{-1}) and power density P (W kg^{-1}) of the SSCs were calculated according to eqn S2 and S3:

$$E = \frac{1}{2}C\Delta V^2 \times \frac{1}{3.6} \tag{S2}$$

$$P = \frac{3600E}{\Delta t} \tag{S3}$$

Where C (F g^{-1}) is the specific capacitance of the SSCs, ΔV (V) represents the potential change within the discharge time Δt (s).

In three-electrode system, the CV curves of L-MoS$_2$ at various scan rates were used to investigate the charge storage mechanism. The peak current density (i) could be obtained from the CV curves at different scan rate (v). Generally, the i and v obey the relationship illustrated in eqn S4 and S5:[1]

$$i = av^b \tag{S4}$$

$$\log i = \log a + b \log v \tag{S5}$$

where a and b can be calculated from $\log i$ versus $\log v$ curves. The charge storage mechanism of electrode could be predicted by the value of b, and b is usually in the range of 0.5-1. The value of b near 0.5 represents the diffusion-controlled process, while the value of b close to 1 indicates the capacitive process. If the value of b is in the range of 0.5-1, the electrode material reveals both diffusion-controlled process and capacitive process.[2]

The charge storage contribution ratio of capacitive process and diffusion-controlled process at a particular scan rate for L-MoS$_2$ can be quantitatively calculated by using the eqn S6 and S7:[3]

$$i = k_1 v + k_2 v^{1/2} \tag{S6}$$

$$i/v^{1/2} = k_1 v^{1/2} + k_2 \tag{S7}$$

where $k_1 v$ and $k_2 v^{1/2}$ respectively refers to the contribution from capacitive process and diffusion-controlled process.

The leakage current of SSCs was recorded during a 2 h potentiostatic holding after the devices were galvanostatically charged to the working voltage of 1.0 V with 0.1 A g^{-1} constant current density. The self-discharge of SSCs was measured via charging to the working voltage of 1.0 V with 0.1 A g^{-1} constant current density. Once the SSC device was fully charged, disconnected the circuit and recorded the change of open circuit voltage with time to determine the self-discharge.

2. Figures
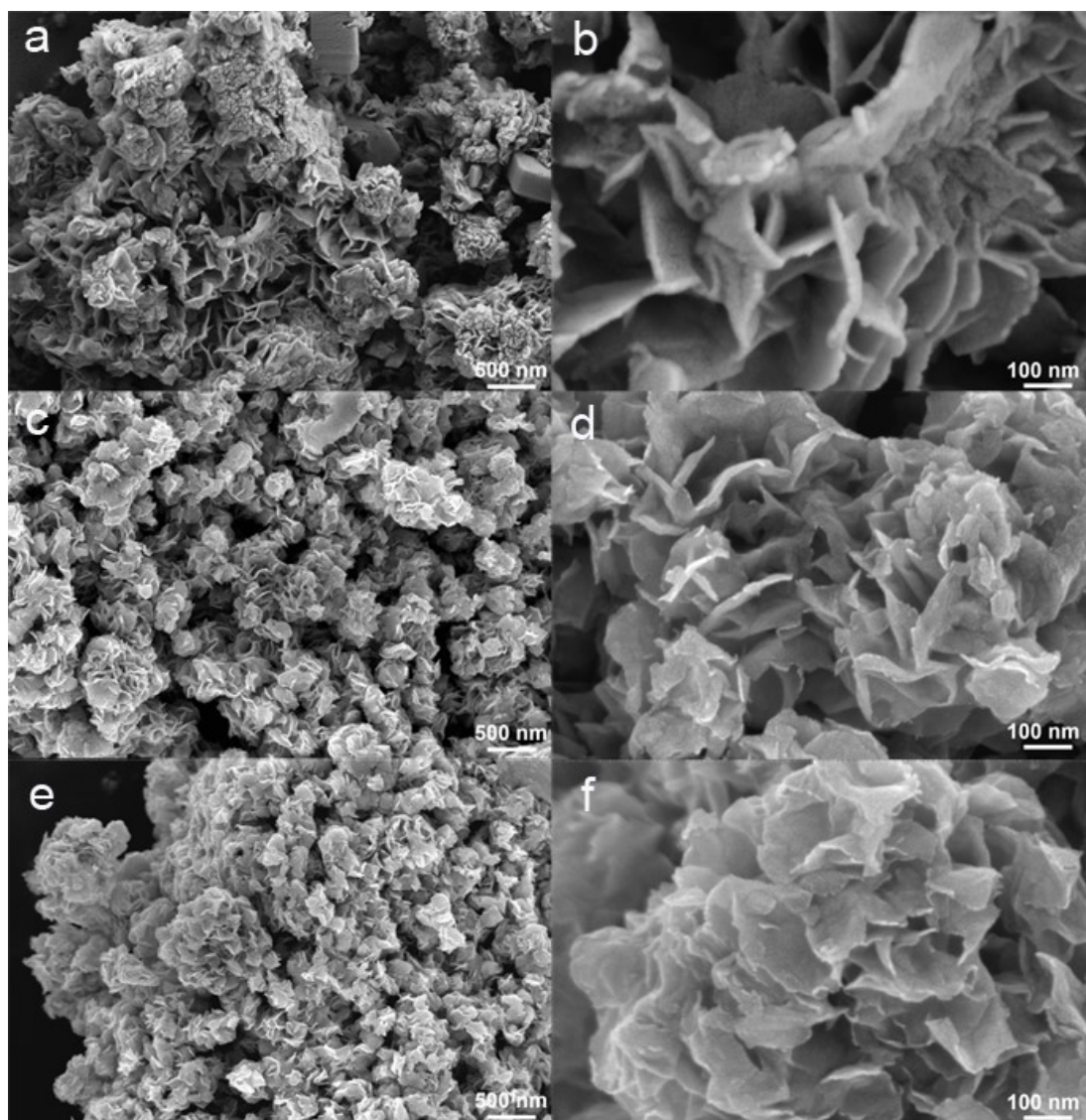
Fig. S1 SEM images of (a, b) MoS_2, (c, d) $L-MoS_2-2.5$ and (e, f) $L-MoS_2-7.5$.
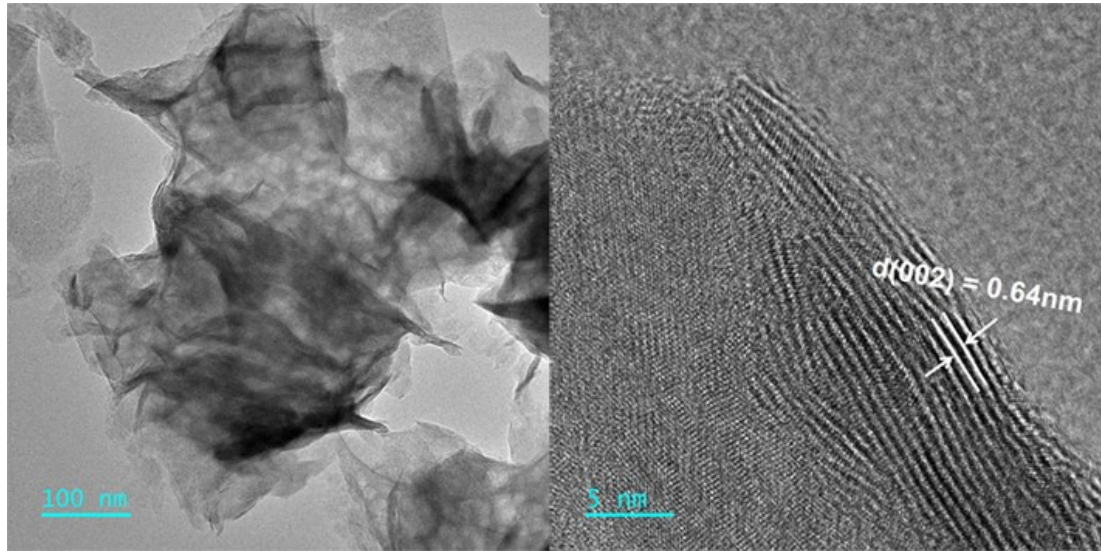
Fig. S2 TEM images of MoS$_2$.
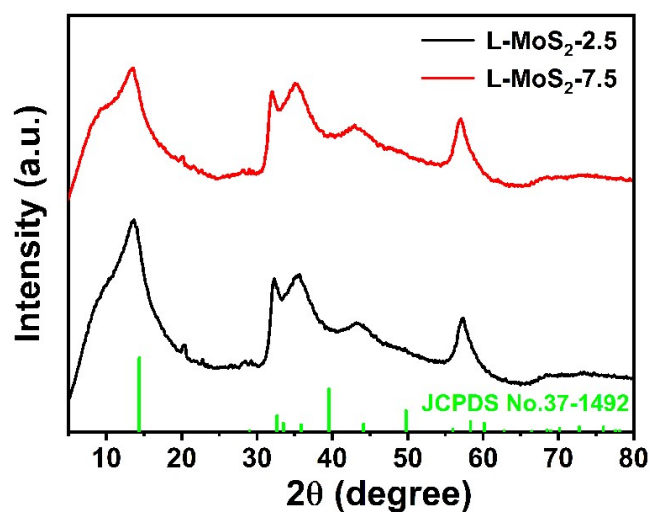
Fig. S3 XRD patterns of L-MoS$_2$-2.5 and L-MoS$_2$-7.5.

In Fig.S3, L-MoS$_2$-2.5 and L-MoS$_2$-7.5 exhibits a characteristic diffraction peak at 2θ of 13.64° and 13.64°, respectively, which can be indexed to the (002) plane of 2H-MoS$_2$. According to the Bragg equation, the (002) plane interlayer spacing of L-MoS$_2$-2.5 and L-MoS$_2$-7.5 is respectively calculated to be 6.42 and 6.53 Å.
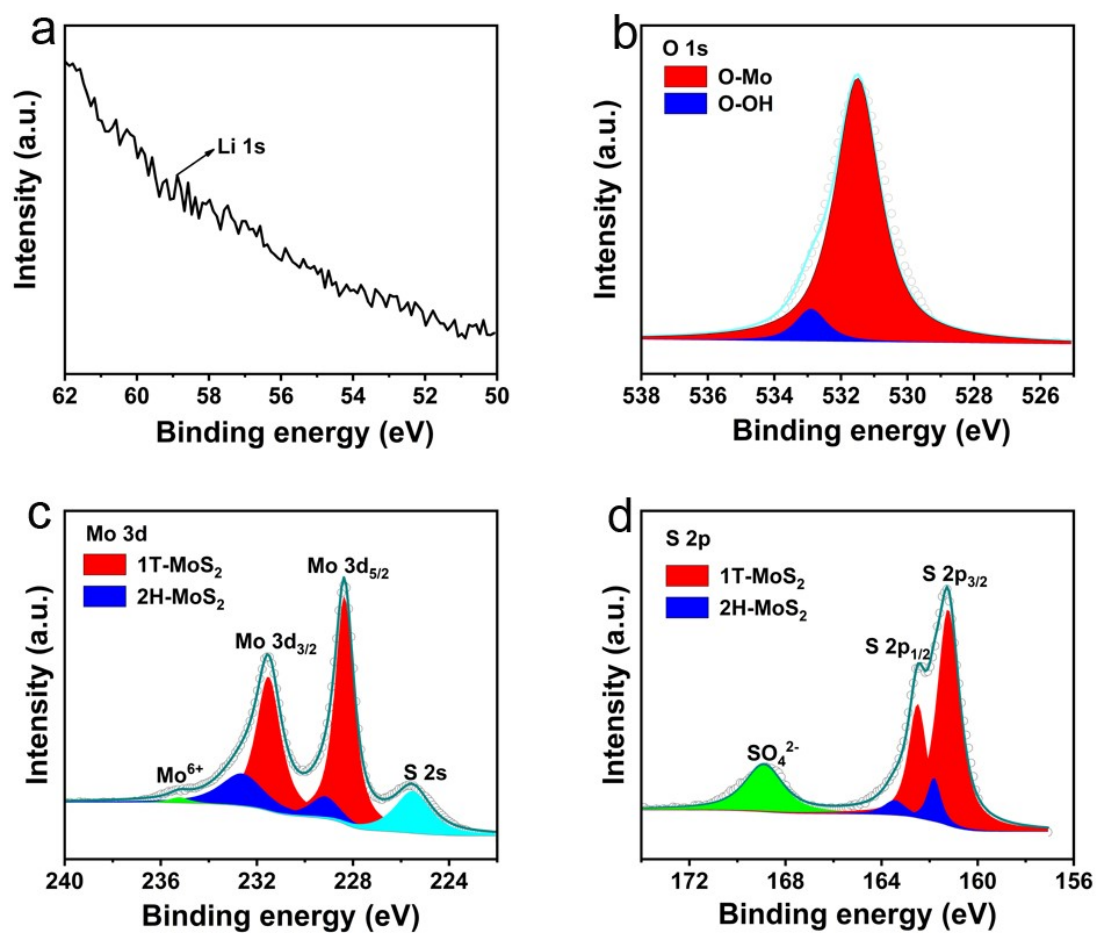
Fig. S4 The high-resolution (a) Li 1s and (b) O 1s XPS spectrum of L-MoS$_2$. The high-resolution (c) Mo 3d and (d) S 2p XPS spectrum of MoS$_2$.
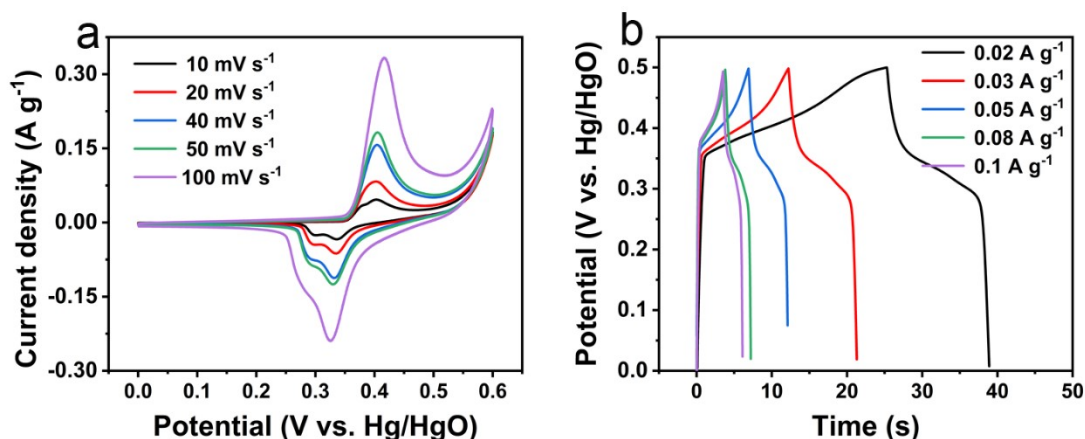
Fig. S5 Electrochemical performances of nickel foam in three-electrode system. (a) CV curves at different scan rates. (b) GCD curves at different current densities.

In this work, nickel foam was used as a current collector. We first studied the electrochemical performance of nickel foam in three-electrode system. In Fig. S5a, the CV curves of nickel foam exhibit distinct redox peaks, which could be attributed to the generated $Ni(OH)_2$ after immersing nickel foam in 2 M KOH solution. In Fig. S5b, the GCD curves of nickel foam are nearly symmetric. At the current density of 0.02 A g^{-1}, the discharge time is 13.5 s, corresponding to the specific capacitance of 0.56 F g^{-1}. At the current density of 0.1 A g^{-1}, the discharge time is only 2.5 s, referring to the specific capacitance of 0.54 F g^{-1}. It is noteworthy that the GCD curve of nickel foam is unable to disclose at the current density of 1 A g^{-1}. However, the lowest current density of GCD tests for L-MoS$_2$ and MoS$_2$ is 1 A g^{-1} in this work, in other words, the contribution of nickel foam to capacitance could be negligible.
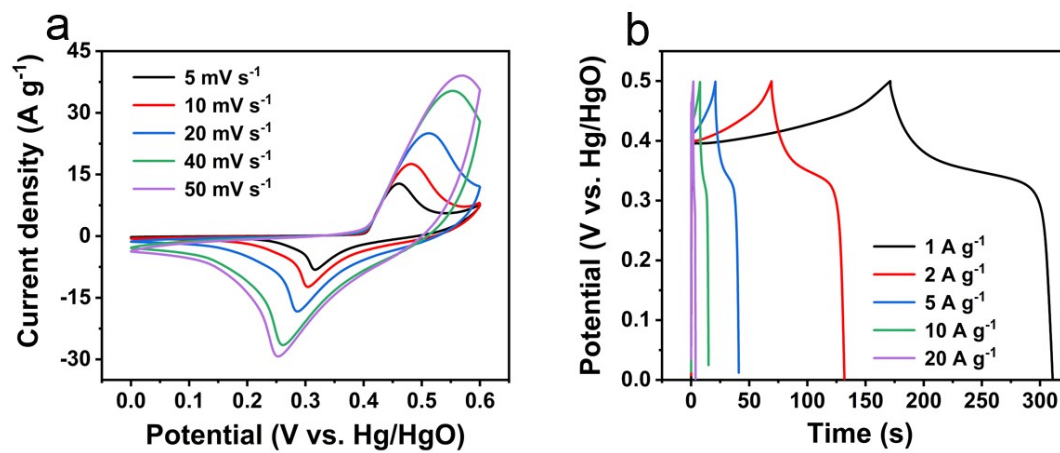
Fig. S6 Electrochemical performance of MoS_2 in three-electrode system. (a) CV curves at different scan rates. (b) GCD curves at different current densities.
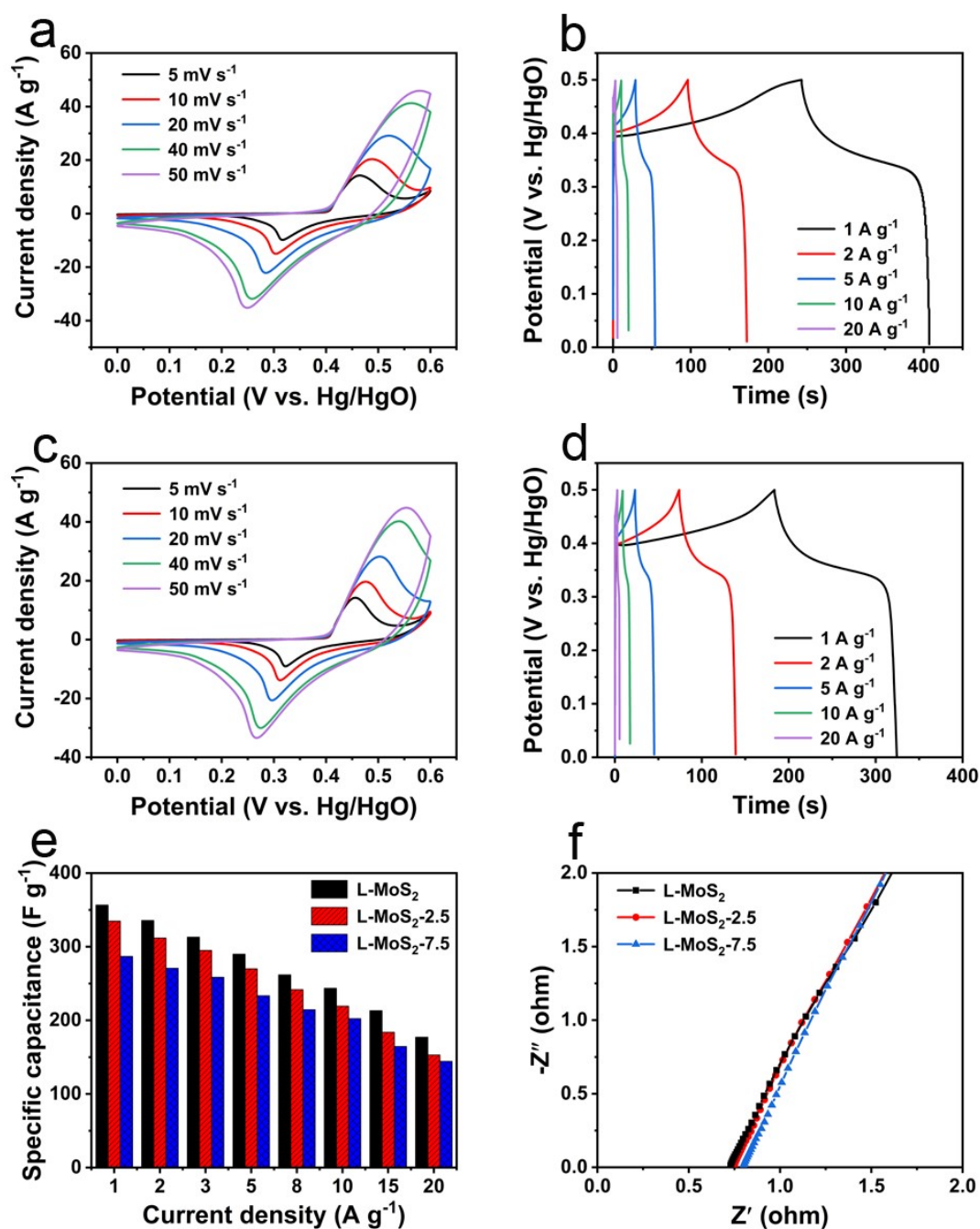
Fig. S7 (a) CV and (b) GCD curves of L-MoS$_2$-2.5. (c) CV and (d) GCD curves of L-MoS$_2$-7.5. (e) Specific capacitance versus current density curves of L-MoS$_2$, L-MoS$_2$-2.5 and SP-MoS$_2$-7.5. (f) Nyquist plots.

In Fig. S7e, L-MoS$_2$-2.5 displays a specific capacitance of 334.8 F g^{-1} at a current density of 1 A g^{-1} and 152.9 F g^{-1} at 20 A g^{-1}, while L-MoS$_2$-7.5 exhibits a specific capacitance of 286.9 F g^{-1} at 1 A g^{-1} and 144.4 F g^{-1} at 20 A g^{-1}. In Fig. S7f, the R$_s$ of L-MoS$_2$, L-MoS$_2$-2.5 and L-MoS$_2$-7.5 is 0.73 Ω, 0.75 Ω, and 0.80 Ω, respectively.
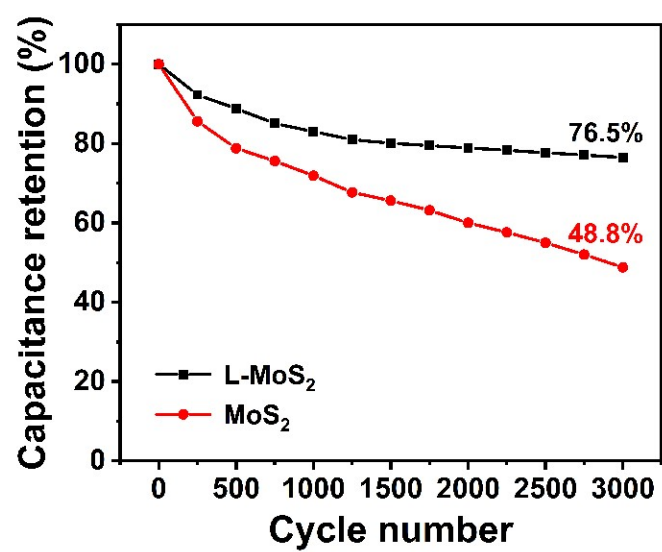
Fig. S8 Cycling stability of L-MoS$_2$ and MoS$_2$ after 3000 cycles at 10 A g^{-1}.
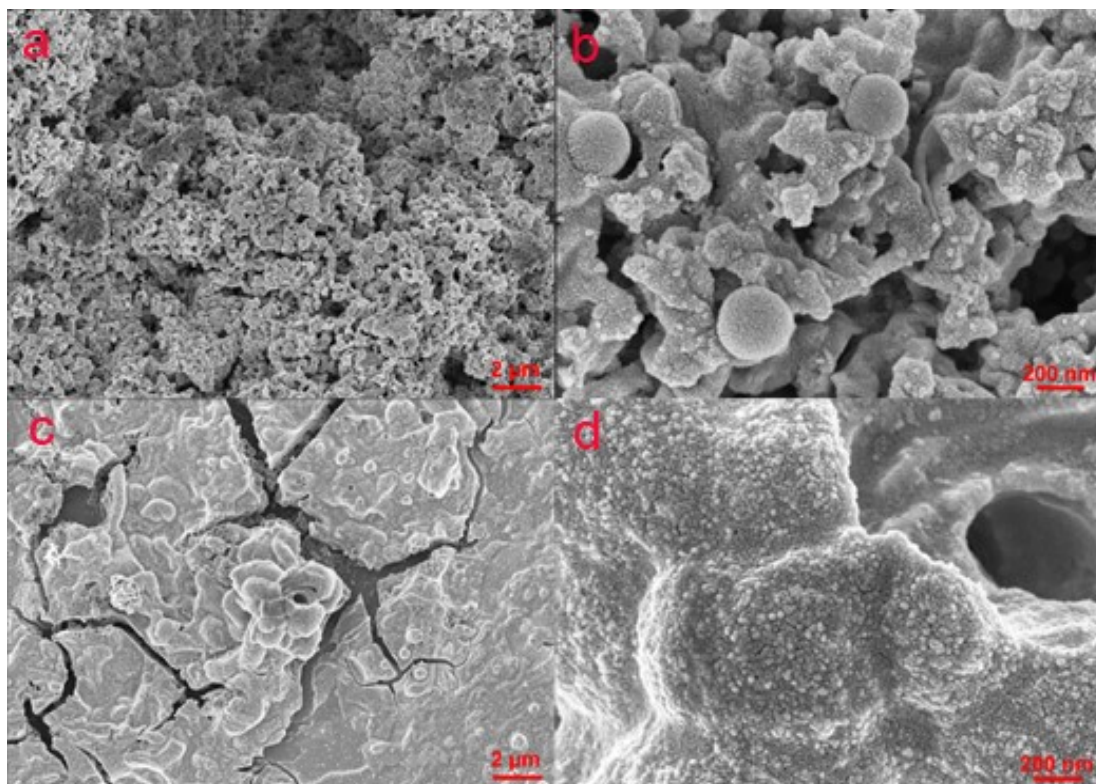
Fig. S9 The SEM images of L-MoS$_2$ electrode (a, b) and MoS$_2$ electrode (c, d) after 3000 cycles at 10 A g^{-1}.

In Fig. S9a and S9b, L-MoS$_2$ electrode still exhibits a porous architecture after 3000 cycles at 10 A g^{-1}. However, L-MoS$_2$ breaks its nanoflower structure and gradually becomes adhesive fragments due to the repeated charge/discharge cycles. In comparison, MoS$_2$ electrode reveals a dense structure and appears several cracks after 3000 cycles at 10 A g^{-1}, as shown in Fig. S9c. The enlarge image in Fig. S9d indicates that MoS$_2$ losses its nanosheet structure and completely turns into nanoparticles after repeated charge/discharge cycles. Compared with MoS$_2$ electrode, the loose and porous nature of L-MoS$_2$ electrode is conducive to generating good cycling stability.

Table S1 Comparative electrochemical performances of MoS_2-based electrodes in literature reports with our work.

Electrode material	Electrolyte	Specific capacitance	Rate Capability	Cycling stability
MoS_2 nanosheets[4]	1 M Li_2SO_4	119.38 F g^{-1} at 5 mV s^{-1}	53.70 F g^{-1} at 100 mV s^{-1}	95.1% after 2000 cycles
LE-MoS_2 nanorods[5]	1 M Na_2SO_4	231 F g^{-1} at 1 A g^{-1}	~155 F g^{-1} at 10 A g^{-1}	76.6 % after 1000 cycles
E-MoS_2 microflowers[6]	1 M Na_2SO_4	246.8 F g^{-1} at 0.5 A g^{-1}	125.0 F g^{-1} at 5 A g^{-1}	70 % after 3000 cycles
MoS_2/NCQDs[7]	1 M Na_2SO_4	379.5 F g^{-1} at 0.5 A g^{-1}	269.7 F g^{-1} at 10 A g^{-1}	82 % after 5000 cycles
MoS_{2-x} nanosheets[8]	1 M Na_2SO_4	170.2 F g^{-1} at 0.5 A g^{-1}	91.8 F g^{-1} at 5 A g^{-1}	87.1 % after 5000 cycles
MoS_2(Synergism)[9]	1 M Na_2SO_4	392 F g^{-1} at 1 A g^{-1}	~200 F g^{-1} at 10 A g^{-1}	87.1 % after 5000 cycles
A-MoS_2[10]	1 M Na_2SO_4	178 F g^{-1} at 1 A g^{-1}	118 F g^{-1} at 5 A g^{-1}	86 % after 5000 cycles
MoS_2 nanoflowers[11]	3 M KOH	1120 F g^{-1} at 1 A g^{-1}	648 F g^{-1} at 20 A g^{-1}	96 % after 2000 cycles
MoS_2/N-CNTs[12]	6 M KOH	225 F g^{-1} at 1 A g^{-1}	90 F g^{-1} at 5 A g^{-1}	89 % after 10000 cycles
Cu doped MoS_2[13]	6 M KOH	353 F g^{-1} at 1 A g^{-1}	267 F g^{-1} at 10 A g^{-1}	94 % after 5000 cycles
L-MoS₂ (Our work)	*2 M KOH*	*356.7 F g^{-1} at 1 A g^{-1}*	*243.6 F g^{-1} at 10 A g^{-1} 177.7 F g^{-1} at 20 A g^{-1}*	*76.5% after 3000 cycles*
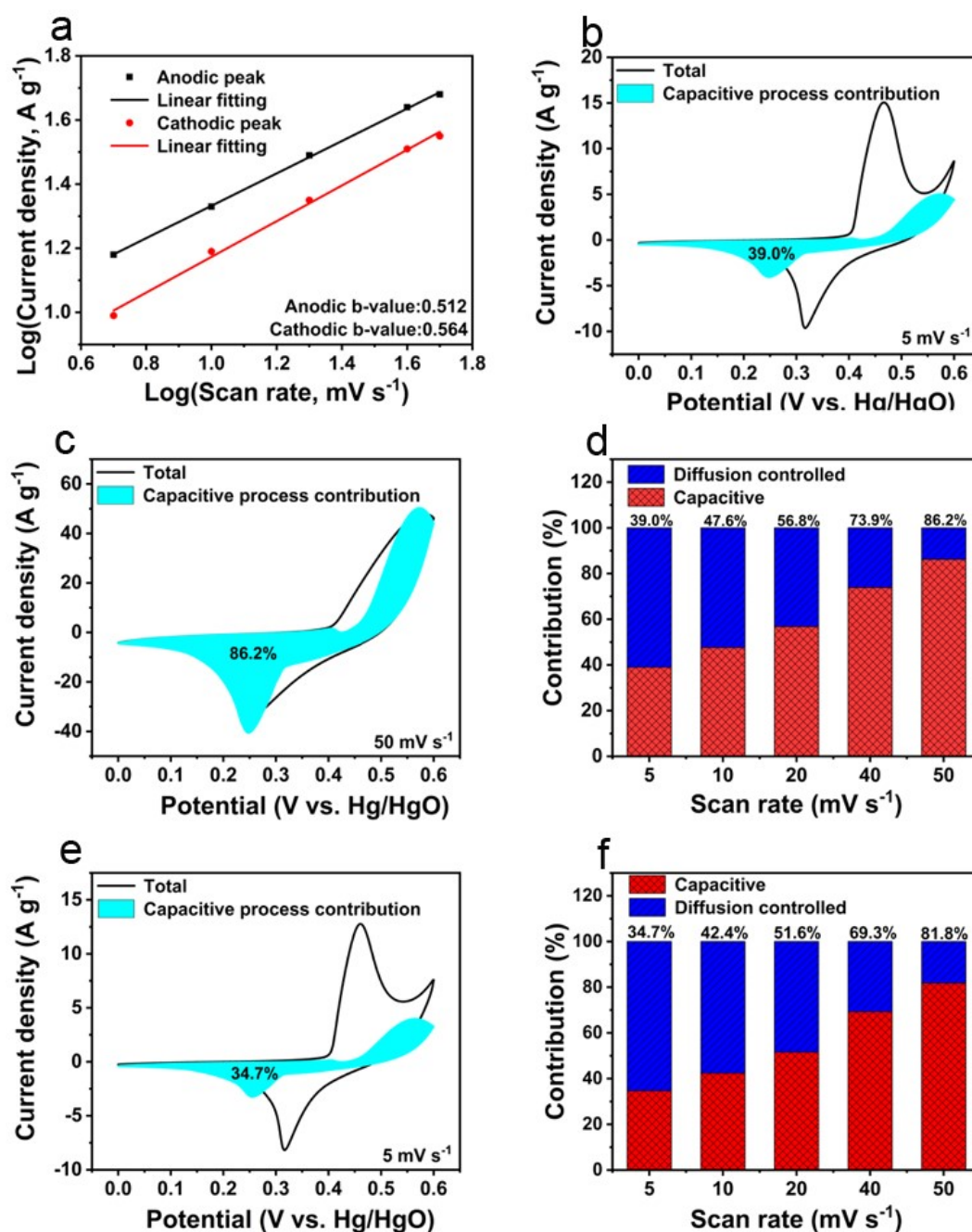
Fig. S10 (a) Log (anodic and cathodic peak current densities) versus log (scan rate) curves of L-MoS$_2$. Capacitive process charge storage contribution of L-MoS$_2$ at (b) 5 mV s^{-1} and (c) 50 mV s^{-1}. (d) Capacitive and diffusion-controlled charge storage contribution ratios of L-MoS$_2$ at various scan rates. (e) Capacitive process charge storage contribution of MoS$_2$ at 5 mV s^{-1}. (f) Capacitive and diffusion-controlled charge storage contribution ratios of MoS$_2$ at various scan rates.
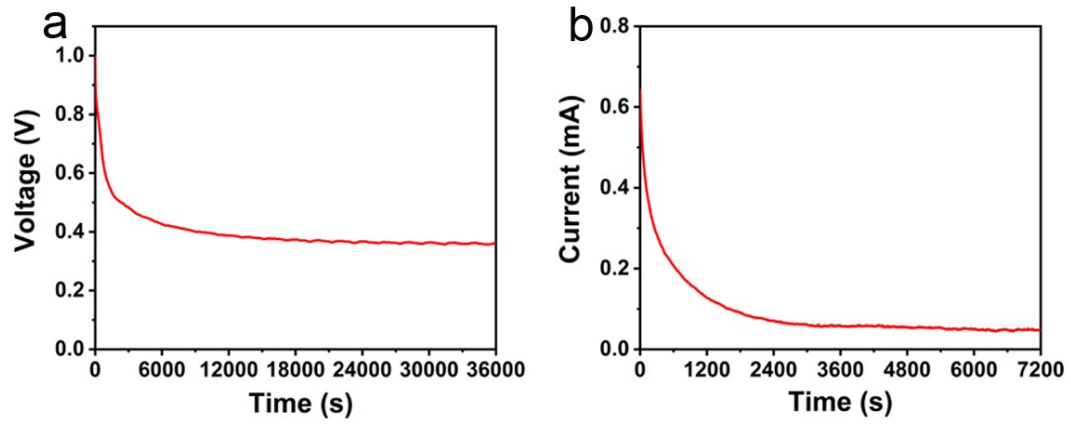
Fig. S11 (a) Self-discharge and (b) Leakage current curves of L-MoS$_2$ SSC device.

References

1 F. Wan, X. Wang, C. Tang, C. Jiang, W. Wang, B. Li, Y. Zhang and X. Zhu, *J. Mater. Chem. A*, 2022, **10**, 12258-12268.

2 Z. Tang, J. Dai, W. Wei, Z. Gao, Z. Liang, C. Wu, B. Zeng, Y. Xu, G. Chen, W. Luo, C. Yuan and L. Dai, *Adv. Sci.*, 2022, **9**, 2201685.

3 W. Hou, Y. Sun, Y. Zhang, T. Wang, L. Wu, Y. Du and W. Zhong, *J. Alloys Compd.*, 2021, **859**, 157797.

4 D. Kesavan, V. K. Mariappan, P. Pazhamalai, K. Krishnamoorthy and S. J. Kim, *J. Colloid Interface Sci.*, 2021, **584**, 714-722.

5 H. Xiao, S. Wang, S. Zhang, Y. Wang, Q. Xu, W. Hu, Y. Zhou, Z. Wang, C. An and J. Zhang, *Mater. Chem. Phys.*, 2017, **192**, 100-107.

6 J. Wang, X. Zheng, Y. Dong, L. Chen, L. Chen and W. He, *Dalton Trans.*, 2023, **52**, 4537-4547.

7 K. Yang, Z. Luo, D. Shu, F. Yi, Z. Zhu and A. Gao, *J. Electroanal. Chem.*, 2022, **908**, 116093.

8 H. Wang, X. Xu and A. Neville, *RSC Adv.*, 2021, **11**, 26273-26283.

9 H. Li, H. Li, Z. Wu, L. Zhu, C. Li, S. Lin, X. Zhu and Y. Sun, *J. Mater. Sci. Technol.*, 2022, **123**, 34-40.

10 X. Sun, Y. a. Pang, S. Li, Y. Yu, X. Ding, L. Wang and Q. Zhang, *Ceram. Int.*, 2022, **48**, 21317-21326.

11 S. Wei, R. Zhou and G. Wang, *ACS Omega*, 2019, **4**, 15780-15788.

12 W. Liu, W. Zhang, S. Zuo, C. Yao and X. Li, *J. Mater. Sci.: Mater. Electron.*, 2021, **32**, 27184-27197.

13 D. Vikraman, S. Hussain, K. Karuppasamy, A. Kathalingam, E.-B. Jo, A. Sanmugam, J. Jung and H.-S. Kim, *J. Alloys Compd.*, 2022, **893**, 162271.